PAPER

Check for updates

Interface engineering of heterogeneous transition metal chalcogenides for electrocatalytic hydrogen evolution

Ruru Song,[a] Deyu Li,[a] Yafeng Xu,[a] Junfeng Gao, [ID][b] Lu Wang [ID] *[a] and Youyong Li [ID] *[ac]

MoS$_2$ and MoSe$_2$ are recognized as promising electrocatalysts for the hydrogen evolution reaction (HER), but the active sites are mainly located on the edge, limiting their electrochemical efficiency. Here we have introduced the 2H-1T' interface structures in MoSSe and MoS$_2$–MoSe$_2$ heterostructures to enhance the HER activity in the basal planes by using the density functional theory (DFT) calculations. The structural stability and electronic properties of different 2H-1T' interface structures are investigated and the HER activities are evaluated by using the H adsorption free energy (ΔG_H). The H adsorption free energy along the interface boundaries is very close to zero, and the optimal sites for the HER are the S or Se atoms, which are bonded with three Mo atoms and located in the center of a hexagonal ring composed of three Mo atoms and three halogen atoms. Our study provides a different approach to activate the basal planes and efficiently improve the electrochemical HER performance of transition metal dichalcogenide materials.

Introduction

As an alternative energy source for fossil fuels, hydrogen energy has some advantages, *i.e.*, cleanliness, high combustion calorific value, diverse storage and transportation methods, and earth-abundant raw materials for preparation. Among the common industrial production methods of hydrogen, electrocatalytic splitting of water to produce hydrogen is considered as the safest and greenest way.[1–3] Noble metals (such as platinum) are usually used as high-efficiency catalysts in the hydrogen evolution reaction (HER),[4,5] but their high-cost limits their large-scale application in industry. Therefore, searching for low-cost and high-efficiency electrocatalysts has become an emerging target in the field of hydrogen production.

Two-dimensional (2D) nanomaterials have attracted the attention of researchers due to their unique structures and electronic properties.[6–8] As a representative of two-dimensional materials, MoS$_2$ has important applications in different fields due to its unique nature. As an electrocatalyst, MoS$_2$ is proved to exhibit advanced catalytic performance for the hydrogen evolution reaction.[9–13] However, many studies have shown that

the active center of MoS$_2$ for the HER is mainly located at the edge, and its basal plane with a large area is inert,[14,15] which greatly limits its application in the field of electrochemical hydrogen production.[16] Thus, activating the sites in the basal plane is necessary for MoS$_2$ to improve the HER performance. Some achievements have been successfully made to improve the catalytic activity for the HER, such as defect modulation[17–19] and chemical doping.[20–22] Introducing phase transition boundaries is also an efficient way to activate the active sites in the basal plane of MoS$_2$. The most stable structure of MoS$_2$ is the 2H phase, while the 1T (1T') phase of MoS$_2$ is metastable but with more active sites.[23] In experiments, the 2H phase could transform into the metallic 1T' phase through various methods, such as lithium intercalation,[24,25] covalent functionalization,[26,27] and direct electron injection.[28] Our previous theoretical study has shown that the basal plane of MoS$_2$ for the HER could be successfully activated by introducing 2H/1T'structural interfaces.[29]

2D transition metal dichalcogenide (TMD) materials can be assembled into heterostructures, and many distinctive properties of these heterostructures have been discovered.[30,31] Heterostructure materials could be divided into vertical heterostructures and planar heterostructures. Janus MoSSe is a kind of vertical heterostructure, which is successfully synthesized by different methods in the literature.[32,33] Theoretical studies have also shown that the introduction of vacancies and grain boundaries could enhance the active sites in the basal plane of the Janus MoSSe surface.[34] The planar heterostructures are also reported between MoS$_2$ and MoSe$_2$, which are

[a]Institute of Functional Nano & Soft Materials (FUNSOM), Jiangsu Key Laboratory for Carbon-Based Functional Materials & Devices, Soochow University, Suzhou, Jiangsu, 215123, China. E-mail: lwang22@suda.edu.cn; yyli@suda.edu.cn

[b]Key laboratory of Material Modification by Laser, Ion and Electron Beams (Dalian University of Technology), Ministry of Education, Dalian, 116024, China

[c]Macao Institute of Materials Science and Engineering, Macau University of Science and Engineering, Taipa, 999078, Macau SAR, China

synthesized by the chemical vapor deposition (CVD) growth method,[35] and exhibit distinguished properties with the high surface area, the improved synergistic effect and a narrow bandgap.[36] Therefore, in our work, we have systematically investigated the active sites and the underlying catalytic mechanism for the HER in the TMD heterostructures from the first-principles calculations, and we found that the phase interface could activate the active sites in the basal plane and efficiently improve the HER performance of the TMD heterostructures.

Computational details

All the calculations were performed with density functional theory (DFT) using the projector-augmented wave method[37] and carried out in the Vienna *Ab initio* Simulation Package (VASP).[38,39] The Perdew–Burke–Ernzerhof (PBE)[40] functional of the generalized gradient approximation (GGA)[41] was adopted to describe the electron exchange–correlation interactions, and the Grimme's scheme of D3 was used to describe the van der Waals interaction and to account for London dispersion interactions.[42,43] The kinetic cutoff energy is set to 450 eV. A vacuum of 15 Å was used to avoid the interactions between layers. The supercell combining 4×4 2H-MoSSe and 4×4 1T′-MoSSe is constructed as the interface model for vertical heterostructures, while the supercell combining 4×4 MoS_2 and 4×4 $MoSe_2$ is used to represent the interface model for planar heterostructures. The Monkhorst–Pack method was used for sampling the Brillouin zone with sufficiently accurate k-points for different sizes of supercells.[44] The lattice constants and atomic positions for all the interface structures were fully relaxed until the force on each atom was under 0.03 eV Å^{-1}.

The Gibbs free energy (ΔG_H) for H adsorption is obtained by:

$$\Delta G_H = \Delta E_H + \Delta E_{ZPE} - T\Delta S \tag{1}$$

where ΔE_H describes the H adsorption energy on the interface structures, ΔE_{ZPE} and ΔS are the differences for the zero-point energy and entropy, and T is the room temperature which is 298.15 K.

We have considered two structural phases in the heterostructure interface, and the formation energy depends on the chemical potential of the S atom, which is defined as:

$$G_f = E_{2H-1T'} + \Delta m \times \mu_s - E_{2H} \tag{2}$$

where $E_{2H-1T'}$ and E_{2H} are the DFT energies of the 2H structure with and without the embedded 1T′ domain, respectively, μ_s is the chemical potential of S, and Δm is the number of S atoms gained or lost at the interface.

The formation energy is contributed by two parts: (i) the formation energy of two different boundaries ($\gamma_{b_1}, \gamma_{b_2}$) formed in heterostructures, and (ii) energy difference between 2H and inserted 1T′ phases. Therefore, G_f can also be written as:

$$G_f = \gamma_{b_1} + \gamma_{b_2} + \Delta E_{1T'-2H} \times n \tag{3}$$

where $\Delta E_{1T'-2H}$ is the energy difference between 2H and 1T′ phases for each chemical unit, and n is the number of units. Combining eqn (2) and (3), we could obtain the formation energies of two isolated boundaries for each heterostructure, which could well evaluate their structural stability.

Results and discussion

2H-1T′ interface structures of MoSSe

According to the previous study,[29] the 2H/1T′ interface structures of TMD materials along the zigzag (ZZ) direction are more stable than those along the armchair direction. So here we only considered the zigzag interface structures formed between 2H and 1T′ phases of MoSSe. It should be noted that there are three typical models that we have considered, and each heterostructure contains two different interface structures, as shown in Fig. 1. The name of our interface structures is defined by the different atomic species (S, Se or Mo) terminated at the ZZ edge from the 2H or 1T′ phase. For example, the $ZZ_{Mo-S/Se}$ interface is formed by the Mo atoms from the 2H phase bonded to the S/Se atoms from the 1T′ phase, and the ZZ_{Mo-Mo} interface is formed between the Mo-terminated 2H phase and the Mo-terminated 1T′ phase. To balance the computational expenses and the necessary separation of 2H and 1T′ phases, we choose the widths of the 1T′ phase in $ZZ_{Mo-S/Se}$–$ZZ_{S/Se-Mo}$, ZZ_{Mo-Mo}–$ZZ_{S/Se-Mo}$ and $ZZ_{S/Se-Se}$–ZZ_{Mo-Mo} interface structures as 17.4 Å, 16.3 Å and 21.8 Å, respectively, which are large enough to provide the remarkable interface boundaries. To compare the relative structural stability, we define the formation energy for these heterostructures, which is described in detail in the
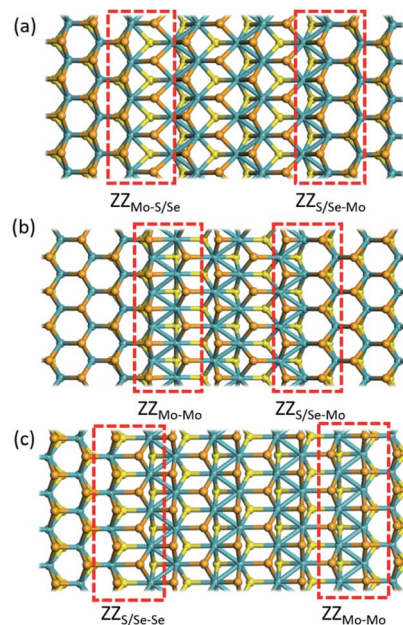

Fig. 1 Optimized structures for the 2H/1T′ interfaces of Janus MoSSe (a) $ZZ_{Mo-S/Se}$–$ZZ_{S/Se-Mo}$, (b) ZZ_{Mo-Mo}–$ZZ_{S/Se-Mo}$, and (c) $ZZ_{S/Se-Se}$–ZZ_{Mo-Mo}. The dashed line indicates the phase boundary of 2H and 1T′ of Janus MoSSe. The cyan, yellow and orange balls represent Mo, S and Se atoms respectively.

computational method. The definition of formation energies has the limitation that we could only obtain the stability of each heterostructure instead of each interface boundary, because each heterostructure contains two different interface boundaries. The formation energies of three MoSSe heterostructures are 2.554 eV, 3.032 eV and 6.675 eV, respectively. Among them, the $ZZ_{Mo\text{-}Mo}$–$ZZ_{S/Se\text{-}Mo}$ interface structure containing two boundaries of $ZZ_{Mo\text{-}Mo}$ and $ZZ_{S/Se\text{-}Mo}$ is the most stable. The $ZZ_{S/Se\text{-}Se}$–$ZZ_{Mo\text{-}Mo}$ interface structure exhibits the highest formation energy with the same species bonded with each other at the interface boundaries.

It is also critical to understand the electronic properties of 2H-1T′ MoSSe structures for their further applications. The band structures and density of states (DOS) of 2H-1T′ MoSSe heterostructures are plotted in Fig. 2, together with the 2H-MoSSe structure. 2H-MoSSe is a direct semiconductor with a band gap of 1.64 eV. By introducing the interface boundaries, all the three 2H/1T′ MoSSe structures become metallic with the new states emerging around the Fermi level. The DOS further proves this and the new states are mostly contributed from Mo atoms. The conductivity of 2H/1T′ MoSSe structures is greatly enhanced, which facilitates the further electrochemical application.

2H-1T′ interface structures between MoS$_2$ and MoSe$_2$

Besides the 2H-1T′ interface existing in MoSSe, we also considered the 2H-1T′ interface structures for planar heterostructures between MoS$_2$ and MoSe$_2$. We have constructed six different interface structures, as shown in Fig. 3. The interface structures formed by 2H-MoS$_2$ and 1T′-MoSe$_2$ are shown in Fig. 3a–c, while those formed between 1T′-MoS$_2$ and 2H-MoSe$_2$ are shown in Fig. 3–f. The definition of their names is the same as that of 2H-1T′ MoSSe interfaces.

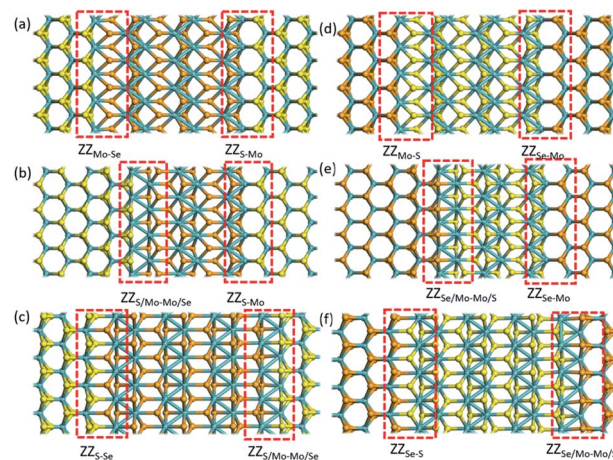**Fig. 3** Optimized structures of 2H-1T′ interfaces between MoS$_2$ and MoSe$_2$. The cyan, yellow and orange balls represent Mo, S and Se atoms, respectively.

We have also compared the formation energies for these 2H-1T′ interface structures between MoS$_2$ and MoSe$_2$. With the same geometrical structure, the interface boundaries formed between 2H-MoS$_2$ and 1T′-MoSe$_2$ are all more energetically favorable than those formed between 2H-MoSe$_2$ and 1T′-MoS$_2$. Among them, the $ZZ_{Mo\text{-}Se}$–$ZZ_{S\text{-}Mo}$ interface structure containing two boundaries of $ZZ_{Mo\text{-}Se}$ and $ZZ_{S\text{-}Mo}$ is the most stable with the lowest formation energy of 2.571 eV. The formation energies for the structures shown in Fig. 3b and c are 3.301 and 6.897 eV, respectively. The interface structures formed between 2H-MoSe$_2$ and 1T′-MoS$_2$ are relatively less stable with the formation energies of 5.235, 7.759 and 8.132 eV, respectively, corresponding to the structures shown in Fig. 3d–f. Similar to the electronic properties of 2H-1T′ MoSSe structures, the interface structures of planar heterostructures formed between MoS$_2$ and MoSe$_2$ also exhibit metallic properties, and the plot of density of states is displayed in Fig. 4. The density of states has shown that the Mo atoms are directly bonded with both S and Se atoms, and some electron states emerge around the Fermi level, which are dominated by the Mo atoms.

HER activity

It is known that the HER is an electrochemical process involving multiple steps. In order to obtain the maximum reaction rate, the Gibbs free energy of H* adsorption (ΔG_H) on the catalyst surface should be close to zero, so here we employ the ΔG_H to evaluate the HER activity on these interface structures. The more negative the ΔG_H value is, the stronger the H atom adsorption on the catalyst, making it difficult to separate out, while the more positive ΔG_H values indicate that the H atom is difficult to adsorb. We have systematically screened all the possible adsorption sites of H atoms on the 2H-1T′ interface structures that we have considered here. The H adsorption on the pristine 2H-MoSSe, 2H-MoS$_2$ and 2H-MoSe$_2$ is very weak with the ΔG_H values of 1.754 eV, 1.873 eV and 1.990 eV, respectively, indicating a very poor HER performance on the
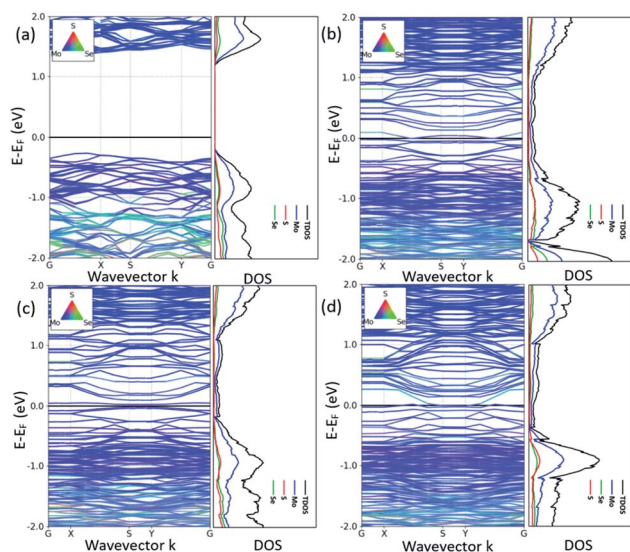

Fig. 2 Band structures and density of states of 2H-1T′ MoSSe heterostructures, together with the 2H-MoSSe structure. The black line indicates the Fermi level.
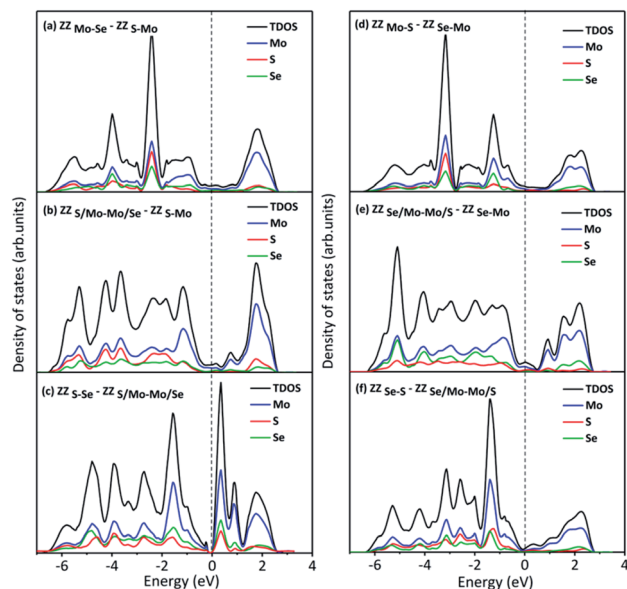
Fig. 4 Density of states of 2H-1T′ interface structures formed between MoS_2 and $MoSe_2$, which corresponds to the structures shown in Fig. 3. The dashed line indicates the Fermi level.

basal plane. By introducing the interface boundaries, the ΔG_H values for the adsorption sites along the interface boundaries are very close to zero, which is shown in Fig. 5a and c.

Different from the previous studies on pristine MoSSe and MoS_2, whose active sites are the Mo sites at the edge, H prefers to bind to the S or Se atoms located at the 2H-1T′ interfaces. For the 2H-1T′ MoSSe interface, there are optimal sites for H adsorption on ZZ_{Mo-Mo}, $ZZ_{Mo-S/Se}$, $ZZ_{S/Se-Mo}$ and $ZZ_{S/Se-Se}$ boundaries, which are comparable or even better than those of the vacancies and grain boundaries of the 2H-MoSSe surface. It

is worth noting that the ΔG_H values for H adsorbed on S sites of ZZ_{Mo-Mo} and $ZZ_{Mo-S/Se}$, and Se sites of $ZZ_{S/Se-Mo}$ are 0.008 eV, 0.038 eV and 0.07 eV, respectively, which are very close to zero, indicating the high HER performance of the basal plane. For the 2H-1T′ MoS_2–$MoSe_2$ interfaces, there are also some optimal sites with the similar configurations. For example, the ΔG_H on Se sites of ZZ_{S-Mo} and $ZZ_{S/Mo-Mo/Se}$ can reach −0.031 eV and −0.088 eV, respectively, which are the superior active sites in the basal plane for the HER. The optimal active sites exhibit similar geometries, as shown in Fig. 5. The optimal S or Se sites are mostly bonded with three Mo atoms and located in the center of a hexagonal ring composed of three Mo atoms and three S or Se atoms, providing the guideline to design the promising HER electrocatalysts in the future.

The volcano curve is also plotted to further describe the HER performance, and the theoretical exchange current densities (i_0) are calculated by using the obtained ΔG_H results. According to Norskov's assumption,[45] i_0 can be expressed as:

when $\Delta G_H \leq 0$,

$$i_0 = -ek_0\{1/[1 + \exp(\Delta G_H/kT)]\} \qquad (4)$$

when $\Delta G_H > 0$,

$$i_0 = -ek_0\{1/[1 + \exp(-\Delta G_H/kT)]\} \qquad (5)$$

where k_0 is the rate constant for the proton transport in the solution, and k_0 is set to 1. k is the Boltzmann constant and T is the room temperature which is 300 K. The exchange current densities for the H adsorption sites on all the interface structures are calculated and a volcano curve is plotted as shown in Fig. 5b and d. Structures with negative and positive ΔG_H values are located around the left and right sides of the volcano curve, respectively, and the sites with the ΔG_H values close to zero are located around the peak of the volcano plot. Obviously, the ΔG_H values of most adsorption sites on the 2H/1T′ interface are close to 0, which is located at the peak of the volcano map, indicating the enhanced HER performance. The points far away from the peak in the volcano plot are the sites with poor HER performance, which are the relatively inactive sites away from the interface boundaries. These interfaces between 2H and 1T′ phases provide more active sites in the basal plane for the HER and exhibit a relatively high exchange current density.

To explore the underneath reaction mechanism, we have investigated electronic properties of active sites on interface structures with H adsorption. Fig. 6 depicts the projected density of states (PDOS) of the adsorbed H atom, the S or Se atoms bonded with the adsorbed H atom, and three Mo atoms adjacent to the S or Se atoms on pristine 2H-MoSSe and 2H-MoS_2, $ZZ_{Mo-S/Se}$ and ZZ_{Mo-Mo} boundaries in the 2H-1T′ MoSSe interface, and $ZZ_{S/Mo-Mo/Se}$ and ZZ_{S-Mo} boundaries in the 2H-1T′ MoS_2-$MoSe_2$ interface. When H is adsorbed on 2H-MoSSe, the hybridization peak between 1s H and 3p S is located at an energy level of −8.910 eV with a larger positive adsorption free energy of 1.750 eV, which is a very weak interaction between the H atom and substrate. By introducing the 2H-1T′ interface boundaries, the H adsorption is greatly enhanced, and the
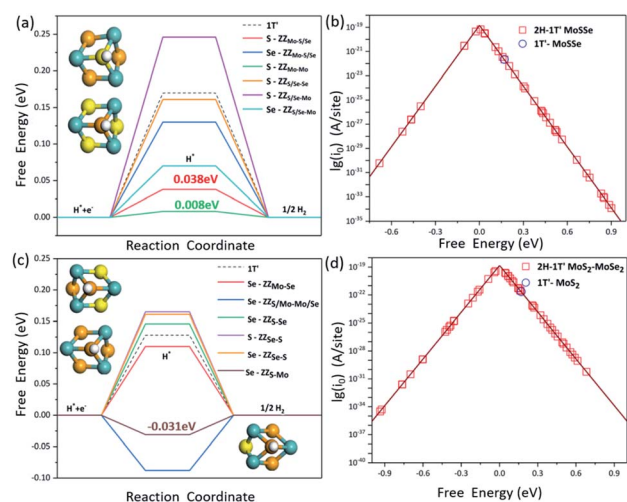

Fig. 5 (a) Gibbs free energies for H adsorption (ΔG_H) on different sites and (b) the plot between the exchange current density i_0 and ΔG_H for 2H-1T′ MoSSe interface structures; (c) ΔG_H on different sites of 2H-1T′ MoS_2−$MoSe_2$ interface structures and (d) the plot between the exchange current density i_0 and the corresponding ΔG_H.
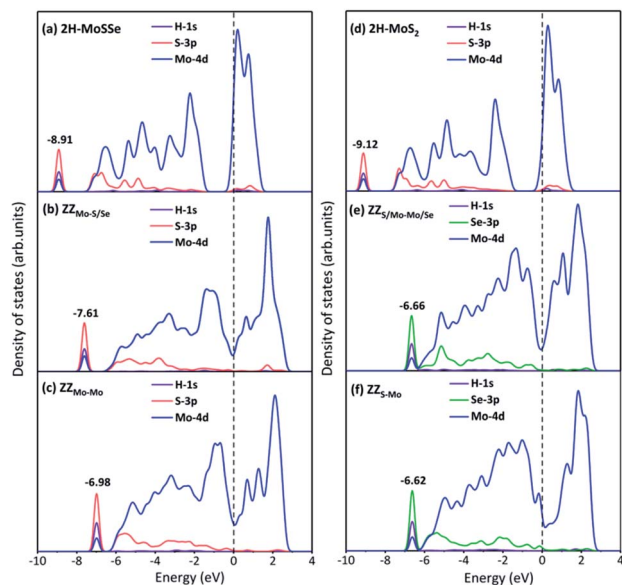
Fig. 6 Projected density of states (PDOS) of H adsorbed on (a) 2H-MoSSe, (b) $ZZ_{Mo-S/Se}$ and (c) ZZ_{Mo-Mo} in 2H-1T′ MoSSe interfaces with the ΔG_H values of 1.750 eV, 0.038 eV and 0.008 eV, respectively; PDOS for H adsorbed on (d) 2H-MoS₂, (e) $ZZ_{S/Mo-Mo/Se}$ and (f) ZZ_{S-Mo} in 2H-1T′ MoS₂–MoSe₂ interfaces with the ΔG_H values of 1.872 eV, −0.088 eV and −0.031 eV, respectively.

hybridization between 1s H and 3p S moves close to the Fermi level. For example, the hybridization peak is located at −7.610 eV and −6.980 eV for $ZZ_{Mo-S/Se}$ and ZZ_{Mo-Mo} in 2H-1T′ MoSSe interfaces, which correspond to the enhanced H adsorption free energies of 0.038 eV and 0.008 eV, respectively. Similar electronic properties are observed in 2H-1T′ MoS₂–MoSe₂ interfaces, as shown in Fig. 6d–f. For 2H-MoS₂, the hybridization peak is located at −9.120 eV with a H adsorption free energy of 1.872 eV. By introducing the 2H-1T′ MoS₂–MoSe₂ interface, the hybridization peaks also shift to the high energy levels of −6.660 eV and −6.620 eV for $ZZ_{S/Mo-Mo/Se}$ and ZZ_{S-Mo} boundaries, respectively, corresponding to the H adsorption free energies of 0.088 eV and 0.040 eV. Therefore, our results have demonstrated that the interface structures could efficiently activate the basal plane of TMD materials and provide abundant active sites in the basal plane for electrocatalytic hydrogen evolution.

Conclusions

In summary, we have investigated the structural and electrocatalytic properties of 2H-1T′ interface boundaries in MoSSe and MoS₂–MoSe₂ heterostructures by using the DFT calculations. The structural stability is compared by using the formation energies, and the ZZ_{Mo-Mo}–$ZZ_{S/Se-Mo}$ interface structure containing two boundaries of ZZ_{Mo-Mo} and $ZZ_{S/Se-Mo}$ is the most stable. All the interface structures are metallic with high electronic conductivity. To evaluate the HER activity, we have calculated the H adsorption free energies on all the possible sites of these interface structures. The optimal sites with the H

adsorption free energies very close to zero are the S or Se sites instead of Mo sites, which are bonded with three Mo atoms and located in the center of a hexagonal ring composed of three Mo atoms and three halogen atoms. The 2H-1T′ interfaces provide more active sites in the basal plane for electrocatalytic hydrogen evolution and exhibit relatively high exchange current density.

Conflicts of interest

There are no conflicts to declare.

Acknowledgements

References

1 J. A. Turner, *Science*, 2004, **305**, 972–974.
2 X. Cheng, Z. Shi, N. Glass, L. Zhang, J. Zhang, D. Song, Z.-S. Liu, H. Wang and J. Shen, *J. Power Sources*, 2007, **165**, 739–756.
3 I. Dincer, *Int. J. Energy Res.*, 2007, **31**, 29–55.
4 S. Trasatti, *J. Electroanal. Chem. Interfacial Electrochem.*, 1972, **39**, 163–184.
5 S. Ye, F. Luo, Q. Zhang, P. Zhang, T. Xu, Q. Wang, D. He, L. Guo, Y. Zhang and C. He, *Energy Environ. Sci.*, 2019, **12**, 1000–1007.
6 D. Voiry, M. Salehi, R. Silva, T. Fujita, M. Chen, T. Asefa, V. B. Shenoy, G. Eda and M. Chhowalla, *Nano Lett.*, 2013, **13**, 6222–6227.
7 C. J. Rupp, S. Chakraborty, J. Anversa, R. J. Baierle and R. Ahuja, *ACS Appl. Mater. Interfaces*, 2016, **8**, 1536–1544.
8 J. Mei, T. Liao, L. Kou and Z. Sun, *Adv. Mater.*, 2017, **29**, 1700176.
9 Y. Li, H. Wang, L. Xie, Y. Liang, G. Hong and H. Dai, *J. Am. Chem. Soc.*, 2011, **133**, 7296–7299.
10 B. Hinnemann, P. G. Moses, J. Bonde, K. P. Jørgensen, J. H. Nielsen, S. Horch, I. Chorkendorff and J. K. Nørskov, *J. Am. Chem. Soc.*, 2005, **127**, 5308–5309.
11 H. I. Karunadasa, E. Montalvo, Y. Sun, M. Majda, J. R. Long and C. J. Chang, *Science*, 2012, **335**, 698–702.
12 Q. Ding, B. Song, P. Xu and S. Jin, *Chem*, 2016, **1**, 699–726.
13 T. F. Jaramillo, K. P. Jørgensen, J. Bonde, J. H. Nielsen, S. Horch and I. Chorkendorff, *Science*, 2007, **317**, 100–102.
14 J. Kibsgaard, Z. Chen, B. N. Reinecke and T. F. Jaramillo, *Nat. Mater.*, 2012, **11**, 963–969.

15 G. Ye, Y. Gong, J. Lin, B. Li, Y. He, S. T. Pantelides, W. Zhou, R. Vajtai and P. M. Ajayan, *Nano Lett.*, 2016, **16**, 1097–1103.

16 M. Bollinger, J. Lauritsen, K. W. Jacobsen, J. K. Nørskov, S. Helveg and F. Besenbacher, *Phys. Rev. Lett.*, 2001, **87**, 196803.

17 J. Xie, H. Zhang, S. Li, R. Wang, X. Sun, M. Zhou, J. Zhou, X. W. Lou and Y. Xie, *Adv. Mater.*, 2013, **25**, 5807–5813.

18 H. Shu, D. Zhou, F. Li, D. Cao and X. Chen, *ACS Appl. Mater. Interfaces*, 2017, **9**, 42688–42698.

19 Y. Ouyang, C. Ling, Q. Chen, Z. Wang, L. Shi and J. Wang, *Chem. Mater.*, 2016, **28**, 4390–4396.

20 J. V. Lauritsen, J. Kibsgaard, G. H. Olesen, P. G. Moses, B. Hinnemann, S. Helveg, J. K. Nørskov, B. S. Clausen, H. Topsøe and E. Lægsgaard, *J. Catal.*, 2007, **249**, 220–233.

21 J. Deng, H. Li, J. Xiao, Y. Tu, D. Deng, H. Yang, H. Tian, J. Li, P. Ren and X. Bao, *Energy Environ. Sci.*, 2015, **8**, 1594–1601.

22 P. Liu, J. Zhu, J. Zhang, P. Xi, K. Tao, D. Gao and D. Xue, *ACS Energy Lett.*, 2017, **2**, 745–752.

23 L. Cai, W. Cheng, T. Yao, Y. Huang, F. Tang, Q. Liu, W. Liu, Z. Sun, F. Hu and Y. Jiang, *J. Phys. Chem. C*, 2017, **121**, 15071–15077.

24 G. Eda, H. Yamaguchi, D. Voiry, T. Fujita, M. Chen and M. Chhowalla, *Nano Lett.*, 2011, **11**, 5111–5116.

25 L. Wang, Z. Xu, W. Wang and X. Bai, *J. Am. Chem. Soc.*, 2014, **136**, 6693–6697.

26 D. Voiry, A. Goswami, R. Kappera, C. d. C. C. e Silva, D. Kaplan, T. Fujita, M. Chen, T. Asefa and M. Chhowalla, *Nat. Chem.*, 2015, **7**, 45–49.

27 Q. Tang and D.-e. Jiang, *Chem. Mater.*, 2015, **27**, 3743–3748.

28 Y. Kang, S. Najmaei, Z. Liu, Y. Bao, Y. Wang, X. Zhu, N. J. Halas, P. Nordlander, P. M. Ajayan and J. Lou, *Adv. Mater.*, 2014, **26**, 6467–6471.

29 N. Zhao, L. Wang, Z. Zhang and Y. Li, *ACS Appl. Mater. Interfaces*, 2019, **11**, 42014–42020.

30 D. Er, H. Ye, N. C. Frey, H. Kumar, J. Lou and V. B. Shenoy, *Nano Lett.*, 2018, **18**, 3943–3949.

31 H. Cai, Y. Guo, H. Gao and W. Guo, *Nano Energy*, 2019, **56**, 33–39.

32 A.-Y. Lu, H. Zhu, J. Xiao, C.-P. Chuu, Y. Han, M.-H. Chiu, C.-C. Cheng, C.-W. Yang, K.-H. Wei and Y. Yang, *Nat. Nanotechnol.*, 2017, **12**, 744–749.

33 J. Zhang, S. Jia, I. Kholmanov, L. Dong, D. Er, W. Chen, H. Guo, Z. Jin, V. B. Shenoy, L. Shi, *ACS Nano*, 2017, **11**, 8192–8198.

34 W. Shi, G. Li and Z. Wang, *J. Phys. Chem. C*, 2019, **123**, 12261–12267.

35 A. Arora, P. K. Nayak, S. Bhattacharyya, N. Maity, A. K. Singh, A. Krishnan and M. R. Rao, *Phys. Rev. B*, 2021, **103**, 205406.

36 D. Monga and S. Basu, *RSC Adv.*, 2021, **11**, 22585–22597.

37 P. E. Blöchl, *Phys. Rev. B*, 1994, **50**, 17953.

38 G. Kresse and J. Furthmüller, *Comput. Mater. Sci.*, 1996, **6**, 15–50.

39 G. Kresse and J. Furthmüller, *Phys. Rev. B*, 1996, **54**, 11169.

40 J. P. Perdew, M. Ernzerhof and K. Burke, *J. Chem. Phys.*, 1996, **105**, 9982–9985.

41 J. P. Perdew, K. Burke and M. Ernzerhof, *Phys. Rev. Lett.*, 1996, **77**, 3865.

42 S. Grimme, J. Antony, S. Ehrlich and H. Krieg, *J. Chem. Phys.*, 2010, **132**, 154104.

43 S. Grimme, S. Ehrlich and L. Goerigk, *J. Comput. Chem.*, 2011, **32**, 1456–1465.

44 D. Chadi, *Phys. Rev. B*, 1977, **16**, 1746.

45 J. K. Nørskov, T. Bligaard, A. Logadottir, J. Kitchin, J. G. Chen, S. Pandelov and U. Stimming, *J. Electrochem. Soc.*, 2005, **152**, J23.